Int. J. Electrochem. Sci., 12 **(2017)** 6404 – 6416, doi: 10.20964/2017.07.43

International Journal of
ELECTROCHEMICAL
SCIENCE
www.electrochemsci.org

Electrochemical and Surface Investigation of Ni-Cr Glassy Alloys in Nitric Acid Solution

Khadijah M. Emran[*], *Hanaa AL-Refai*

Chemistry Department, College of Science, Taibah University, Al-Madinah Al-Monawarah,
Kingdom of Saudi Arabia.
[*]E-mail: kabdalsamad@taibahu.edu.sa

Received: 5 April 2017 / *Accepted:* 11 May 2017 / *Published:* 12 June 2017

To understand the corrosion and passivation behaviour of $Ni_{70}Cr_{21}Si_{0.5}B_{0.5}P_8C_{\leq 0.1}Co_{\leq 1}Fe_{\leq 1}$ (VZ1) and $Ni_{72.65}Cr_{7.3}Si_{6.7}B_{2.15}C_{\leq 0.06}Fe_{8.2}Mo_3$ (VZ2) glassy alloys they were studied in nitric acid at different concentrations (1.0- 12.0 M) by AC and DC techniques. Experimental investigations showed that both two alloys spontaneously passivated with a small active region followed by a well-defined passive and transpassive regions at all examined HNO_3 concentrations. Critical concentration was observed up to 6.0M HNO_3 for VZ1 alloy and up to 3.0M HNO_3 in the case of VZ2 alloy. Surface morphology was also studied by XPS, SEM, EDS, and AFM techniques after electrochemical measurements. The SEM results showed, deep pit propagation and aggressive surface dissolution with high average roughness values at critical concentration for both two alloys. The inner passive film of Cr_2O_3 and outer passive layer of NiO on VZ1 alloy resulting great resistivity.

Keywords: Ni-Cr glassy alloys, HNO_3, Electrochemical study, morphology study.

1. INTRODUCTION

Metallic glasses (BMGs) are considered to be the materials of the future due to the disordered atomic structure and the absence of grain boundaries[1,2]. A good corrosion resistance is considered as one of the advantageous factors for metallic glasses (MGs). It is thought that high corrosion resistance combined with easily formability in super cooled liquid region leads to the outstanding application potentials in place of traditional crystalline metals[3]. Ni-based glassy alloys are considered as one of the most important BMG systems with the unique and unconventional characteristics[4]. Recently, Ni–Cr–metalloid alloys which possess superior corrosion resistance in concentrated nitric acid solution and high temperatures are expected as a potential material for nuclear fuel reprocessing applications[5]. The XPS is an excellent method to study the chemical composition of the oxide formation on electrode surfaces during corrosion (passivation) in different solutions in electrochemical process[6]. Also, the SEM AFM are important techniques to elucidate the surface properties of specimens like surface roughness[7].

The objective of this study was to investigate the electrochemical and passivation properties of two Ni-base glassy alloys in HNO_3 solutions and characterize their surface. Experiments were performed at different concentrations (1.0-12.0M) at 27°C in order to understand the role of the concentration on the behavior of the passive film formation on VZ1 and VZ2 alloys. The surface condition and chemical composition of the alloys surface after cyclic polarization were examined using XPS, SEM equipped with EDS, and AFM.

2. EXPERIMENTAL

Two Ni-based glassy alloys with nominal compositions of $Ni_{70}Cr_{21}Si_{0.5}B_{0.5}P_8C_{\leq 0.1}Co_{\leq 1}Fe_{\leq 1}$ (VZ1) and $Ni_{72.65}Cr_{7.3}Si_{6.7}B_{2.15}C_{\leq 0.06}Fe_{8.2}Mo_3$ (VZ2) (at%) were investigated in this work. The ingots alloys were supplied by Vacuumschmelze. The 25 µm thickness Ni-Cr glassy alloys sheets were evaluated under the same condition with working area (100mm^2). Just one side of the sample was exposed to corrosive environment (the bright face) as working electrode. The other side was coated with epoxy resin. Before each measurement, this working electrode was degreased with acetone, rinsed several times with double distilled water, cleaned in an ultrasonic bath and finally connected to a copper specimen holder and immersed in the test solution. The test electrolytes used in the study were (1.0, 3.0, 6.0, 9.0, and 12.0 M) HNO_3 solutions, which were prepared from reagent grade chemical and double distilled water. The nitric acid was obtained from Aldrich chemical co. The electrochemical measurements were performed in a typical three-compartment glass cells containing three electrodes, the working electrode (WE), which is the alloy under study, the counter-electrode (CE) it is a platinum wire. The reference electrode (RE) is a saturated Ag/AgCl. Electrochemical measurements were conducted by means of an Interface 1000TM, Gamry Potentiostat/Galvanostat/ZRA analyzer.

This system allow to make the electrochemical tests on same sample and same solution using sequencer system. The EIS measurements were carried out with a sinusoidal voltage of 10mV and 10 points per decade. The frequency range was from 800 kHz to 0.1 Hz. Cyclic polarization curves were obtained with a potential sweep rate of 1 mV/s. The potential was sweep from cathodic to anodic directions after impedance run in range from -800 mV to 1.200 mV.

For surface investigation, X-ray photoelectron spectroscopy (XPS) measurements were carried out using a monochromatic Al K α X-ray source operating at 300 W (Kratos Axis Ultra DLD). The surface condition and chemical composition of the alloys surface after cyclic polarization were examined using a JEOL JSM-6000 scanning electron microscope (SEM) equipped with energy dispersive X-ray spectroscopy (EDS) microanalysis hardware with 15 kV. To provide superior topographic images Atomic Force Microscopy (AFM) measurements were carried out using a Veeco digital instrument CP-II(contact mode).

3. RESULTS AND DISCUSSION

3.1. Electrochemical measurements

The complex impedance diagrams spectra, Fig. 1(a), for VZ1 are similar characterized by incompletely resolved arcs. The diameter of the open arc when drawn to make a semicircle would be much larger indicates the resistance of VZ1 alloy in HNO_3 is high[8].

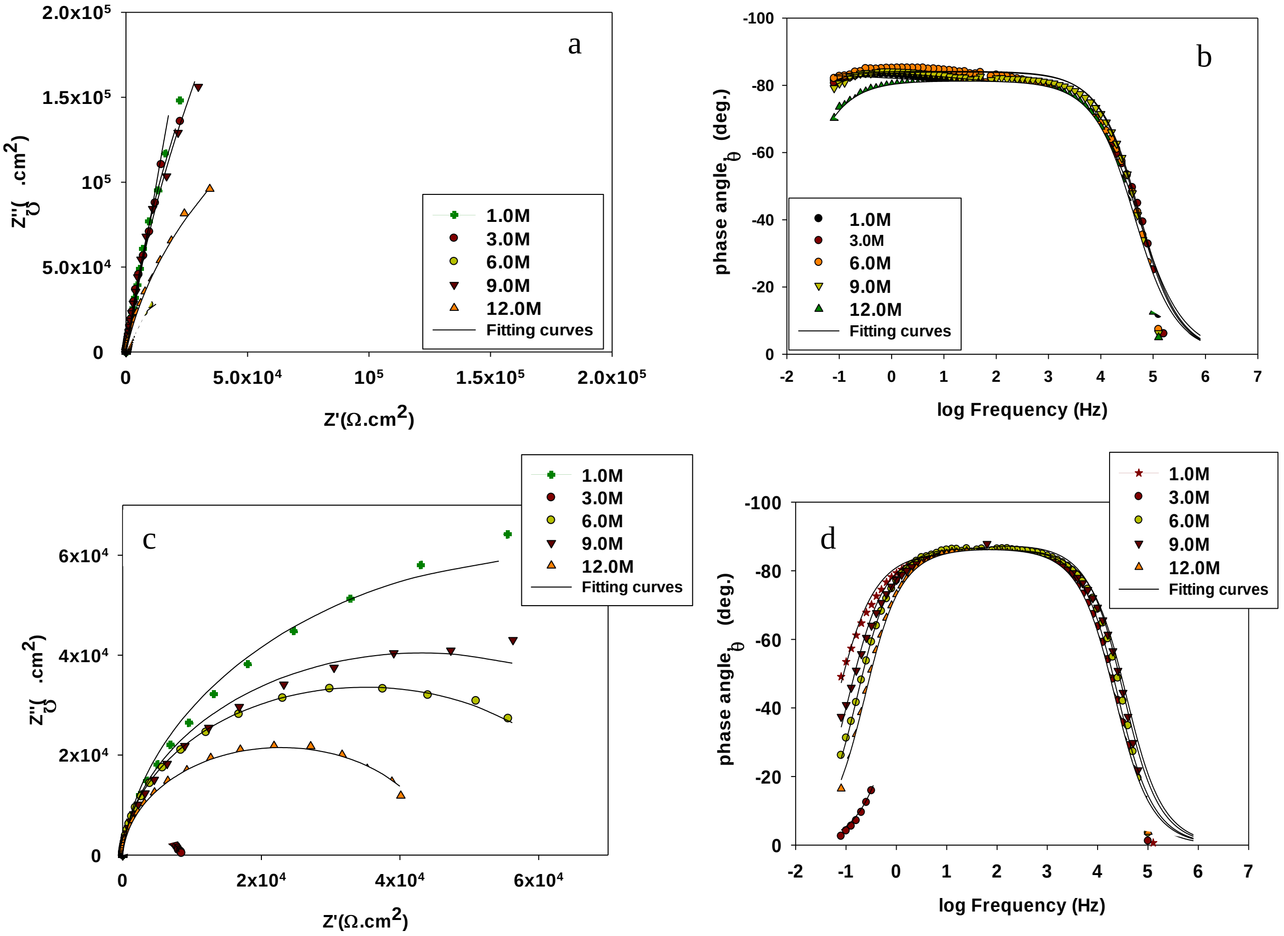

Figure 1. Impedance plots of Ni-base glassy alloys in different concentrations of HNO_3 at 27˚C.

This phenomenon corresponding to a broad phase angle peak in the Bode phase plots, Fig. 1(b), (indicates an interaction of two time constants, reflecting a layered structure of the surface oxide film) and exhibited by all acid concentrations, indicate high resistance of this alloy toward corrosion. Moreover, higher phase angle ($\boldsymbol{\theta}_{max}$) can be noticed close to 90˚ over a wide range from medium to low frequencies. This behavior is attributed to highly capacitive response reflecting typical behavior of passive materials[9]. The arc of the capacitive loops decreases in size, up to 6.0 M and then the arc of the capacitive loops increases. The impedance spectra displaying one constant phase element for VZ2, Fig. 1(c), as most capacitive loops at high frequency are depressed semicircles rather than regular semicircles associated with the roughness of electrode surface. The Warburg impedance in the low frequency indicating the corrosion process involved the transport of reactants from the bulk solution to the alloy/solution interface or transport of soluble corrosion products from the interface to the bulk solution. Moreover, the critical concentration observed at 3.0 M, and then the resistivity increase with further increase of acid concentration until it increased to the maximum in 9.0 M. The size of capacitive arc later reduced at 12.0 M. Bode plots (Fig. 1(d)), exhibited a single peak indicating single time constant with a less depressed semicircle at 1.0M and maximum phase angles close to 90°. This indicates a better quality of the passive layer. At 3.0 M of acid, the value of $\boldsymbol{\theta}_{max}$ reduces to about 82° suggests that the protection quality of the passive layer was poorly. The maximum phase angle return to increase at 6.0 M HNO_3, may be attributed to the high stability of the passive film formed at high acid concentration.

The circuit model (Fig. 2(a)) with the circuit description code (CDC) $R_s(Q_{f/e}R_{f/e})(Q_fR_f)$, displays VZ1 alloy surface with two passive film structure. The first oxide film, at high frequency, was related to an outer porous layer and the second one, at lower frequency was attributed to an inner compact barrier layer[9]. The circuit elements (RC circuits) used in Fig. 2(a) represent impedance responses for the oxide film (R_f), charge transfer processes at the film/electrolyte ($R_{f/e}$) and the solution resistance (R_s) represent the resistance between the working and the reference electrode, ($C_{f/e}$) ;double layer capacitor, and (C_f) passive film capacitor. The results of the fitting parameters are summarized in Table 1. A constant phase element (CPE) was using instead of a pure capacitance (C) in the fitting procedure.

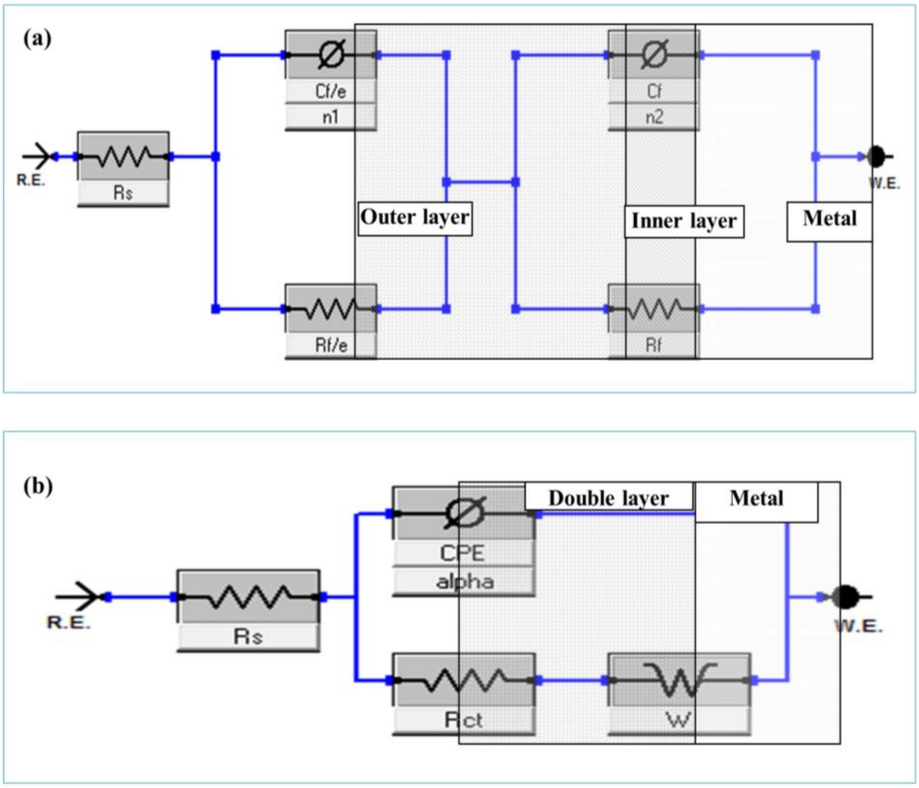

Figure 2. Electrical equivalent circuit used to analyze the present experimental EIS data; (a) VZ1 alloy, (b) VZ2 alloy.

Table 1. Equivalent circuit parameters for the spontaneously formed passive film on VZ1 and VZ2 alloys as a function of HNO_3 concentration at 27˚ C.

Alloy	Con.HNO_3 M	$R_{f/e}$ $\times 10^6\ \Omega\ cm^2$	$C_{f/e}$ $\times 10^{-5}$ F cm^{-2}	n_1	$C_{eff(f/e)}$ $\times 10^{-5}$ Fcm^{-2}	d_1 nm	R_f $\times 10^6\ \Omega\ cm^2$	C_f $\times 10^{-5}$ F cm^{-2}	n_2	$C_{eff(f)}$ $\times 10^{-5}$ Fcm^{-2}	d_2 nm	Total thickness nm
VZ1	1.0	4.841	2.421	0.958	2.983	0.356	392.1	1.260	1.0	1.26	2.11	2.47
	3.0	1.710	4.032	0.839	6.661	0.160	9.630	2.211	1.0	2.21	1.20	1.36
	6.0	0.015	4.383	0.894	8.761	0.121	7.730	2.961	0.935	4.32	0.615	0.736
	9.0	2.271	1.160	0.933	1.471	0.724	5.531	3.168	0.907	5.38	0.494	1.22
	12.0	0.019	2.463	0.891	2.241	0.473	1.015	3.231	0.904	5.89	0.451	0.924
	Con.HNO_3 M	R_{ct} k $\Omega\ cm^2$	C $\times 10^{-5}$ F cm^{-2}	n	C_{eff} $\times 10^{-5}$ Fcm^{-2}	d nm						
VZ2	1.0	128.6	1.801	0.949	1.884	1.41						
	3.0	8.153	1.849	0.930	1.603	1.66						
	6.0	63.41	1.581	0.975	1.581	1.68						
	9.0	82.41	1.332	0.979	1.334	1.99						
	12.0	36.92	1.682	0.958	1.647	1.61						

From Table 1, it can be seen that the $R_{f/e}$ values of VZ1 alloy decreases with increasing concentration of acid up to 6.0 M, and then the resistance occur. The resistance ($R_{f/e}$) increase about 153 and 1.2 time at 9.0 M and 12.0 M respectively compared the resistivity at 6.0 M. This response is a characteristic of passive metals. The $C_{f/e}$ values increase (outer layer) with increasing concentration of acid up to 6.0M. This suggests that the surface roughness caused by corrosion increases the real surface area and double layer capacitance. This is further supported by decreases the n_1 values in proportion to the increase in the HNO_3concentration. The film capacitance C_f increases and R_f decreases with increasing concentration of acid from 1.0 M to 12.0 M indicate the loss of the insulating properties as the barrier layer becomes more defective[10]. The high values of R_f (10^5 -10^8 Ωcm^2) and n_2 (1.0-0.9) indicates that the inner surface film is compact and grows uniformly[11].

The CPE elements are commonly converted into a pure capacitance (C) by means of the following equation Eq.1[12].

$$C_{eff} = \frac{(QR)^{\frac{1}{n}}}{R} \quad (1)$$

where C_{eff} is the effective capacity ($F.cm^{-2}$), R is the charge transfer resistance ($\Omega.cm^2$), Q is the constant phase element ($\Omega^{-1}cm^{-2}s^n$), and n is the surface roughness $1 \geq n \geq 0$.

Assuming surface time-constant distribution, the effective capacity could be calculated by Eq.1, and the corresponding, oxide thickness formed on VZ1alloy can be calculated at different concentration of HNO_3 according to Eq.2. For simplification, the total oxide layer (outer and inner) could possibly be considered as insulator of area A, thickness d, and dielectric constant ε forming capacitor[13]:

$$C_{eff} = \frac{A\varepsilon\varepsilon^o}{d} \quad (2)$$

where d is the average thickness of the protective layer, ε is the dielectric constant of the oxide film (dielectric constant of 12 was adopted for NiO as outer passive layer and 30 for Cr_2O_3 as inner passive film as XPS analysis confirm later), ε^o is the vacuum permittivity ($\varepsilon^o = 8.854 \times 10^{-14}$ Fcm^{-1}) and A is the effective surface area of the electrode (1 cm^2)[14].

The thickness data in Table 1 reveal that the lower resistivity of VZ1 alloy at 6.0 M due to 0.736 nm of oxide film. This film consists of two layers; the outer layer is porous whereas the inner is a compact one.

The EIS model is represented in Fig. 2(b) for the VZ2 alloy. This model is described with circuit description code (CDC) $R_s(Q(R_{ct}W_z))$ in which R_{ct} represents the charge-transfer resistance, a constant phase element, CPE (Q), related to the double layer capacitance, W_z the Warburg impedance and R_s the solution resistance. Results of the fitting parameters are summarized in Table 1. The R_{ct} values in Table 1 decrease sharply from 128.6 kΩcm^2 to 8.153 kΩcm^2 with increase in acid concentration from 1.0 M to 3.0 M. Then the R_{ct} values were increased from 63.4 kΩcm^2 to 82.4 kΩcm^2 with increase in acid concentration from 6.0 to 9.0 M, while the C_{dl} values tend to decrease in the same trend. These results demonstrate that the formation of a protective passive layer (at concentration up to 3.0M) on the electrode surface leads to decreases electrical capacity of the double layer between the charged alloy surface and the electrolyte. This because they displace the water molecules adsorbed on the alloy surface and acts as a barrier to the diffusion of H^+ ions from solution to electrode surface. The thickness of this protective layer increases with increase in acid concentration until reach the maximum value at 9.0M (1.99nm), slowing down the corrosion rate. At 12.0 M the R_{ct} value was reduced about 36.9 kΩcm^2, indicating the passive film becomes more defective at high acid concentration.

Cyclic polarization curve for 1.0 M HNO_3 was presented to gain more information about the dissolution and passivation behaviour for the studied specimens VZ1 and VZ2 alloys at ambient temperature. The curves recorded for other concentration were similar and have been omitted for better clarity of the figures. For VZ1 alloy (Fig. 3a), the curve shows typical active – passive behavior with a small active region followed by a well-defined passive and transpassive regions at all examined HNO_3 concentrations[15]. Moreover, brown gases (nitrogen gases) can be observed at relatively low pH, due to the series of the cathodic reactions of the reduction of nitric acid occurs according to (Eq. 3)[16,17]:

$$NO_3^- \rightarrow NO_2 \rightarrow NO_2^- \rightarrow NO + N_2 \quad (3)$$

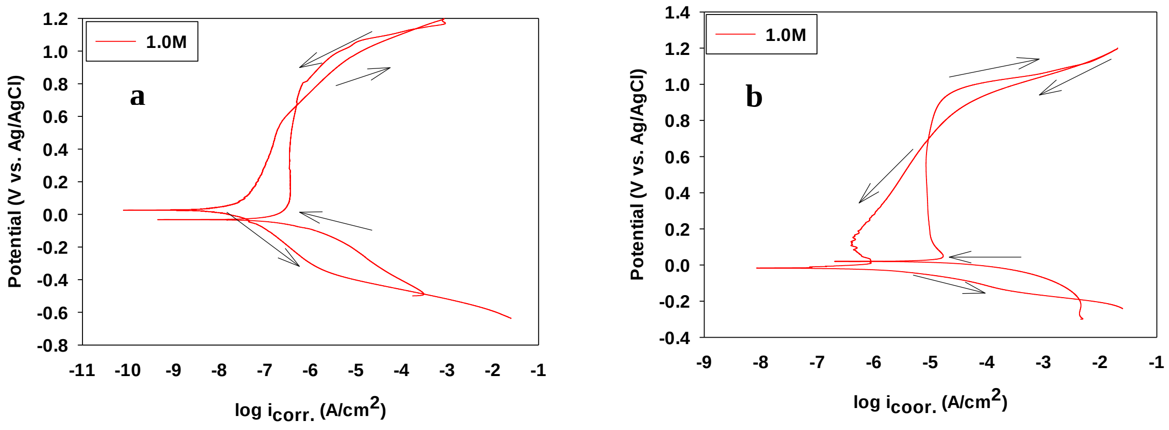

Figure 3. Cyclic polarization curves of Ni-based glassy alloy at 1.0 M HNO_3 at 27°C. (a) VZ1, and (b) VZ2 alloys.

When the anodic polarization starts, alloy dissolute and causes increase the current in the active region. As the potential increases, the rate of the anodic current decreases and the alloys spontaneously passivated at low potential. Moreover, the current plateau was observed very dependent on the acid concentration. At high potential, the polarizing current increases rapidly above the breakdown potential in the transpassive region with parallel polarization curves at all acid concentrations. This indicated that the dissolution process occurs with the same mechanism. It can be observed that VZ1 alloy exhibited high resistance by having high break down potential (E_b), and repassivation potential (E_{rep}) values, This is related to transpassive dissolution or possible due to oxygen evolution according to (Eq. 4) or local passivity breakdown of passive films, resulting in localized corrosion of the alloy.

$$2H_2O \rightarrow 4H^+ + O_2 + 4e^- \quad (4)$$

Electrochemical parameters associated with cyclic polarization measurements, such as corrosion potential (E_{corr}), corrosion current densities (i_{corr}) and cathodic Tafel slope (β_c), break down potential (E_b), and repassivation potential (E_{rep}) are summarized in Table 2. Due to existence of passivation in conjunction with a dissolution reaction and absence of linearity in anodic branch, the corrosion current density (i_{corr}), which is equivalent to the corrosion rate was calculated by Tafel extrapolation of cathodic polarization curve alone to the corrosion potential (E_{corr})[9,15]. This method usually produces a longer and better defined Tafel region[16]. It can be noticed from Table 2 that the E_{corr} values shifted to more positive indicating the enhancing of anodic process and the passive region becomes successively smaller with the increase in HNO_3 concentration. Critical behavior is observed after 6.0 M of acid where the alloy resistance increases as the acid concentration increases about 42.2 and 11.9 time at 9.0 and 12.0 M respectively compared the resistivity at 6.0 M. This resistivity due to the rate of oxide growth for VZ1 alloy increases at these two concentrations as discussed in impedance part. A small positive hysteresis can be observed on the portion of the reverse scan in Fig. 3a. It reflects the small disruption of surface passivity and the ease in restoring passivity as the potential is decreased back toward the corrosion potential at constant scan rate[18]. The passive current density (i_{pass}) of VZ1 alloy is very low indicating the surface oxide layer has a highly protective nature, probably due to its very low ionic/electronic conductivity[8].

The physicochemical processes that occur during film growth and dissolution can be described according to point defect model (PDM) that the passive film forms as a bilayer structure comprising. A compact inner layer that forms directly from alloying elements and an outer layer that forms by the hydrolysis of metal cations, by their reaction with anions present in the solution (e.g., H_2O, OH^-, NO_3), or even by reaction of the inner layer with the solution[19,20].

In this case the chromium content of the alloy is sufficiently high, 21%, that is controlling passive behavior with the other alloying elements and enhancing the formation of bilayer passive films showing a duplex structure compounded by an external oxy-hydroxide layer at the oxide/solution interface covering an inner Cr_2O_3 protective and compact layer at the oxide/alloy interface[14,21].

The growth and dissolution of bilayer passive films can be described according to the following reaction Eq.(5-9):

$$Cr + V_{Cr}^{3-} \xrightarrow{k_1} Cr_2O_3 + 3e^- \quad (5)$$

$$\frac{2}{3}Cr+\frac{2}{3}Cr_2O_3\xrightarrow{k_2}V_O^{2+}+2e^- \qquad (6)$$

$$Cr_2O_3\xrightarrow{k_3}V_{Cr}^{3-}+Cr^{3+}(soln.) \qquad (7)$$

$$V_O^{2+}+H_2O\xrightarrow{k_4}Cr_2O_3+2H^+ \qquad (8)$$

$$Cr_2O_3+6H^+\xrightarrow{k_5}2Cr^{3+}(soln.)+3H_2O \qquad (9)$$

where $V_{Cr}^{3-}\equiv(CrO_3)^{3-}$ is cation vacancies which generated at the barrier layer/outer layer interface and consumed at the alloy/barrier layer interface, $V_O^{2+}\equiv(Cr_2O_2)^{2+}$ is anion vacancies which formed at the alloy/barrier layer interface and consumed at the barrier layer/outer layer interface[21]. Film growth continues until the rate of growth equals the rate of film dissolution. Thus, steady state is achieved[21].

Figure 4 shows that, the adsorption of NO_3^- increases the potential difference across the passive film which enhances the rate of metal ions diffusion (Ni^{+2} or/and Cr^{+3}) from the alloy/film interface to the film/solution interface. This leading to enhancement of the cation vacancy penetrate into the metal phase at a slower rate than their transport through the film. The excess cation vacancies accumulate at the metal/film interface. These results in separation of the barrier layer from the alloy, whereas at the regions where the barrier layer is still attached to the alloy, the film continues to grow. The dissolution of the barrier layer at the film/solution interface results in the thinning the cap cover the expanding condensate. Stress of thinning occurring at the point at which vacancy condensation, which lead in turn to pitting on the alloy surface and the breakdown the passive film[20,22].

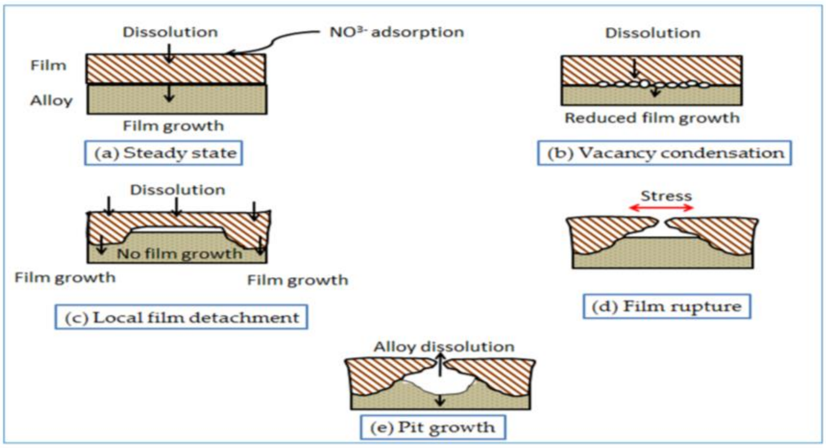

Figure 4. Various stages of pit nucleation according to the point defect model.

The transpassive region started at potentials below the measured potential of oxygen evolution on platinum. In this region (800-1000mV vs. Ag/AgCl), the composition and structure of the passive film change. According to Pourbaix diagram for Cr, the oxidation of chromium (III) to chromium (VI) could produce (H_2CrO_4, CrO_4^{2-}) according to Eqs.10&11 and which activates the surface and causes transpassive dissolution of the passive surface[23].

$$Cr_2O_3 + 5H_2O \rightarrow 2CrO_4^{2-} + 10H^+ + 6e^- \quad (10)$$

$$Cr_2O_3 + 4H_2O \rightarrow Cr_2O_7^{2-} + 8H^+ + 6e^- \quad (11)$$

The VZ2 alloy at 3.0 M showed the highest corrosion rate (130.30 μA cm^{-2}) while at 9.0M showed the lowest corrosion rate (0.8840 μA cm^{-2}) due to the repassivate by re-growth of the oxide film.

Table 2. Electrochemical parameters of polarization for VZ1 and VZ2 alloys in naturally aerated HNO_3 solutions at 27°C.

Alloys	Con.HNO_3 *M*	E_{corr} *mV*	i_{corr} *μA cm^{-2}*	E_{pass} *mV*	E_b *mV*	E_{rep} *mV*	E_{corr}-E_{pass} *mV*	-$β_c$ *mV/decade*	i_{pass} *μA cm^{-2}*	E_b-E_{pass} *mV*	E_{cp}	i_{cp} *μA cm^{-2}*
VZ1	1.0	-29.17	0.232	58.25	700.2	1160	-87.42	100.3	0.297	641.9	-	-
	3.0	188.1	0.431	315.5	830.1	1083	-127.4	115.4	1.071	514.6	-	-
	6.0	454.5	0.908	558.5	946.9	1126	-104.2	107.4	1.961	388.4	-	-
	9.0	556.0	0.022	688.1	1062	1340	-132.1	106.7	0.611	373.9	-	-
	12.0	770.5	0.076	830.1	956.6	1000	-59.61	103.9	0.211	126.5	-	-
VZ2	1.0	19.64	46.10	145.6	932.1	1120	-125.9	60.62	8.185	786.4	58.25	0.171
	3.0	41.96	130.3	179.6	728.8	1116	-137.6	60.71	19.31	549.2	72.82	0.464
	6.0	316.1	1.352	417.5	781.6	1150	-101.4	62.26	3.969	364.1	-	-
	9.0	400.9	0.884	560.7	1014	1169	-159.8	62.47	23.56	453.3	-	-
	12.0	566.7	5.995	666.3	1001	1165	-99.61	64.11	30.37	334.7	-	-

The break down potential E_b increases slightly as concentration increases. This effect can be attributed to the presence of Mo and Cr as alloying elements that enhances the stability of the passive film. The high current density obtained for VZ2 alloy within the range 0.884-130.30 μA cm^{-2} compared to VZ1 alloy within the range 0.0215-0.908 μA cm^{-2} may due to the effect of Ni and/ or Fe in the passive film. The presence Ni and Fe enter the lattice of the passive film making it less protective and so increase the corrosion rate.

3.2. Morphological Study

3.2.1. X-Ray Photoelectron Spectroscopy (XPS) Measurements in Nitric Acid Solution

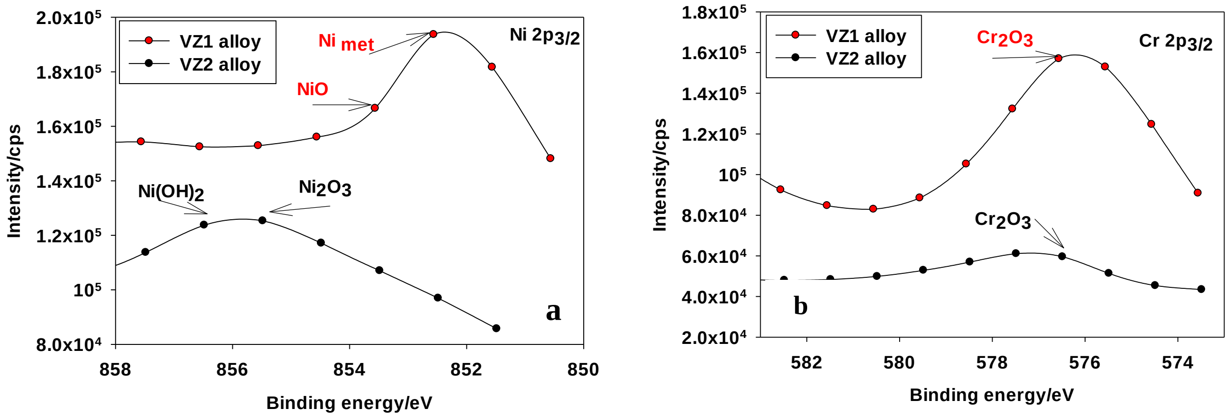

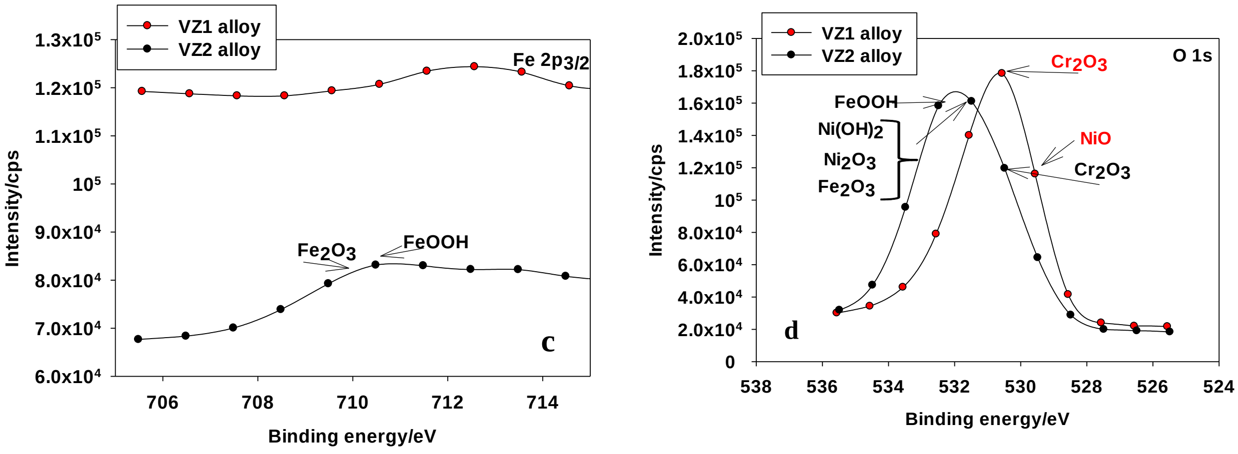

Figure 5. XPS spectra detected for passive film formed on Ni-base glassy alloys in 1.0M HNO_3 at 27°C. (a) Ni $2p_{3/2}$. (b) Cr $2p_{3/2}$. (c) Fe $2p_{3/2}$. (d) O 1s.

The Ni $2p_{3/2}$ spectrum for VZ1 alloy, shows broad peak, representing the metallic state Ni (metal) (852.3eV) and Ni(II) oxide at binding energy about 853.3eV (Fig. 5a). The Cr $2p_{3/2}$ spectrum shows only one peak, indicating the existence of one oxidation state of Cr at about 576.3eV (Fig. 5b). It was assigned to the trivalent (Cr(III)) species of (Cr_2O_3) that formed in the inner passive film. The O 1s for O^{-2} spectrum shows a peak related to binding energy of Cr_2O_3 at 530.3eV and binding energy of NiO at about 529.9eV as outer passive layer (Fig. 5d) [10,24,25]. For VZ2, the peaks showed in Fig.5(a) are related to binding energy of Ni_2O_3 at 855.5eV and $Ni(OH)_2$ at 856.3eV according to the dates in literature[24]. The Cr $2p_{3/2}$ spectrum consisted of one peak at 576.3 eV correspond to Cr_2O_3 (Fig. 5b). The peak at 710.3 eV for Fe^{ox} $2p_{3/2}$ spectrum (Fig. 5c) assigned to Fe_2O_3 and FeOOH[25,26]. The O 1s spectrum at 531.3 eV was assigned to O^{-2} and OH^{-} groups in Ni_2O_3, $Ni(OH)_2$ and Fe_2O_3. The third peak observed at 532.7 eV is attributed to OH^{-}, generally associate with the occurrence of hydrous iron oxides, such as FeOOH(Fig. 5d) [26].

3.2.2 Scanning Electron Microscope, Energy Dispersive X-ray Spectroscopy (SEM /EDS) Analyses and Atomic Force Microscopy (AFM)

The SEM images for VZ1 alloy shown in Fig.6(a,c) exhibited passivating nature and high homogeneous oxide film reflects the high values of n_2 in impedance study (Table 1) indicating the high corrosion resistance[27]. The corresponding EDS spectrum recorded for this passive film is shown in Fig. 6e. In our work, the mass fractions of chemical elements on the film surface (wt%) are as follows: O 19.57, Ni 49.69, Cr 17.11; and atomic fraction (at%): O 40.22, Ni 27.82, Cr 10.82, the atom ratio is about 4:2:1, of which the compositions can be expressed as NiO + CrO_x. For VZ2 alloy, at 9.0 M HNO_3 (Fig. 6b) the SEM shows the compact passive layer formed on the alloy surface which results in the increase in the corrosion resistance. Small pits (at critical concentration) exhibit in the oxide layer formed on VZ2 alloy surface at 3.0 M HNO_3 (Fig. 6d). According to EDS analysis(Fig. 6f), the precipitate is mainly composed of Ni, Cr, O, Si, Fe, Mo, and C in the VZ2 alloy surface. As nitric acid concentration increased the thickness of the corrosion products are growing. This is indicated by the increase of the oxygen content. These results support the results that the corrosion current density show a clear tendency to decrease when HNO_3 concentration increased up to 3.0 M.

Three dimensional (3D) topography images at critical concentration (6.0 and 3.0 M HNO_3 for VZ1 and VZ2 alloy respectively) after cyclic polarization tests are depicted in Fig. 6(g,h). The roughness parameters such as Average roughness (R_a), which gives the deviation in height, maximum profile peak height (R_p), maximum height of the profile (R_T), which gives the vertical distance between the deepest valley and highest peak[28], and the average of these parameters, R_{pm}, and R_{Tm} were obtained and summaries in Table 5. The R_a of VZ1 surface thin films gradually increase upon 6.0 M HNO_3. The films at 6.0 M have the highest value of R_a (3.62 nm) more than other concentration. The distribution will have relatively higher numbers of high peaks and low valleys with a spiky surface[29] and indicate the week properties of the film for alloy protection (as discussed in electrochemical methods).

In the presence of 3.0 M HNO_3 solution, pitting formation was most prominent on the VZ2 alloy surface. Resulted in formation of a highly rough surface (Fig. 6h) with an average roughness value, R_a, of 23.02 nm and a highest peak value, R_p, of 52.35nm (Table 3). This may be explained the worst resistivity at this condition. At 6.0 M HNO_3, the value of average roughness, R_a, decrease and reach the lower value of about 3.43 nm which indicate that the VZ2 alloy has a better corrosion resistance compared to all the testing concentrations.

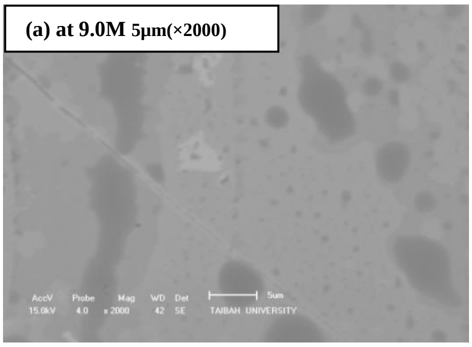

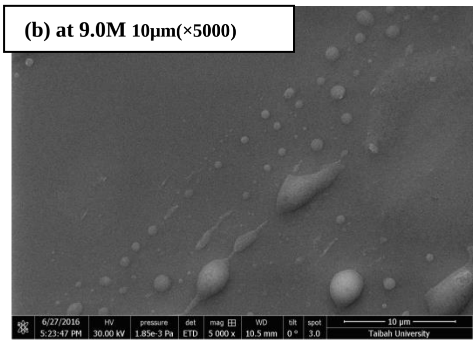

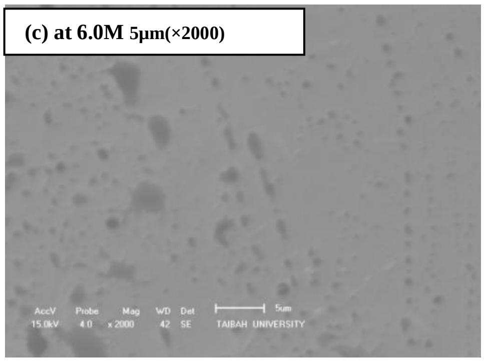

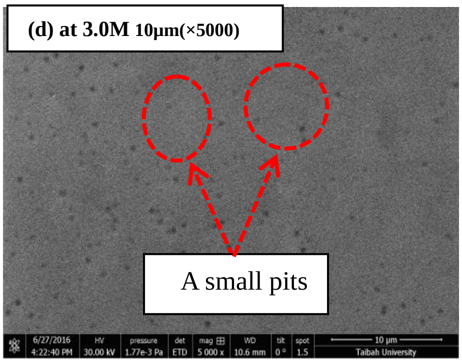

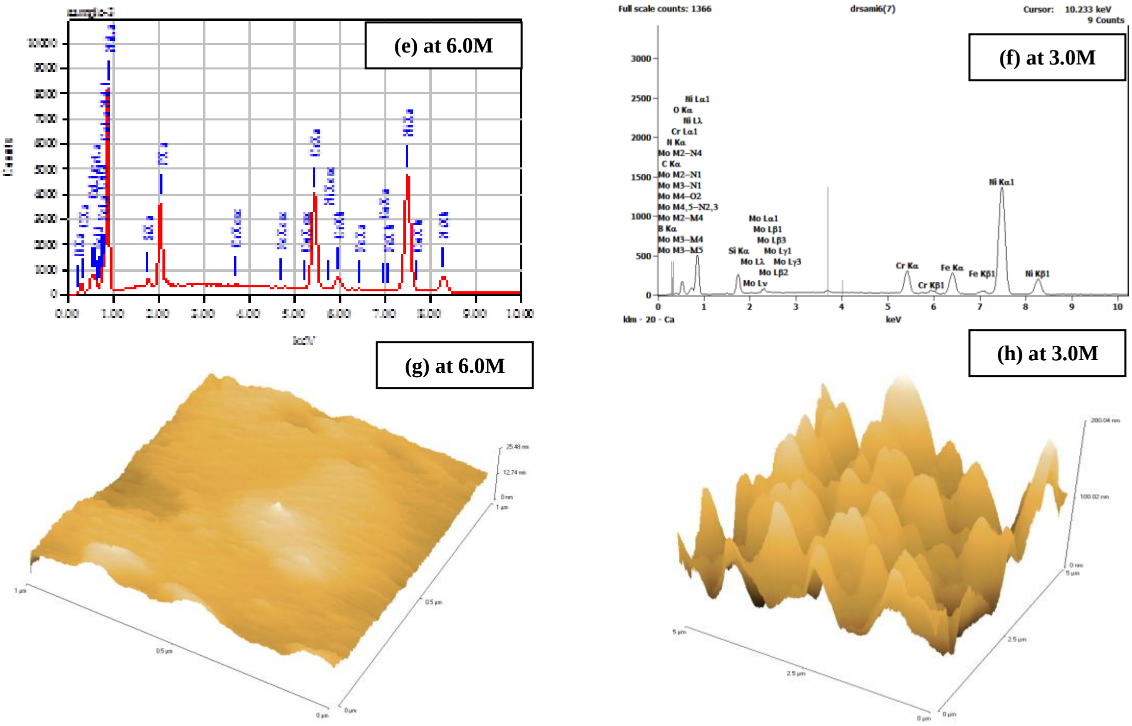

Figure 6. SEM and AFM morphology for Ni-base glassy alloys at different concentration of HNO_3 acid at 27°C.

Table 3. Roughness parameters derived from the AFM images for the VZ1 and VZ2 alloys at 27°C.

Alloys	HNO_3 (M)	R_a (nm)	R_p (nm)	R_{pm} (nm)	R_T (nm)	R_{Tm} (nm)
as-received VZ1alloy	0.0	0.501	1.861	0.882	3.051	1.531
VZ1	1.0	1.111	11.70	3.611	16.71	5.621
	3.0	2.281	18.60	11.64	29.91	18.34
	6.0	3.621	12.63	5.121	22.74	8.612
	9.0	1.352	2.891	1.792	11.90	4.491
	12.0	1.621	3.362	3.261	11.75	4.912
as-received VZ2 alloy	0.0	0.621	1.981	0.899	3.071	1.781
VZ2	1.0	4.372	16.77	7.831	30.52	15.84
	3.0	23.02	52.35	24.00	110.9	51.67
	6.0	3.431	6.521	5.181	32.50	16.30
	9.0	5.141	32.45	9.441	55.69	17.79
	12.0	18.09	53.72	21.28	93.23	44.68

4. CONCLUSIONS

Both two alloys can spontaneously passivate with a small active region followed by a well-defined passive and transpassive regions at all examined HNO_3 concentrations. The alloys exhibited critical concentration up to 6.0M HNO_3 for VZ1 alloy and up to 3.0M HNO_3 in the case of VZ2 alloy. EIS analysis revealed that the VZ1 alloy exhibited higher corrosion resistance when compared to VZ2 alloy. This attributed to the formation of bilayer passive films showing a duplex structure compounded by an outer porous layer at high frequency and an inner compact barrier layer of Cr_2O_3 at lower frequency.

ACKNOWLEDGEMENT
The authors would like to thank Dr.Hartmann Thomas from Vacuumschmelze company for providing the specimens. Also, the authors would like to thank the Kink Abdulaziz City of Science and Technology (KACST) for financially supporting part of this research under Contract (GSP-37-23).

References

1. E. Axinte, *Mater. Des.* 35 (2012) 518.
2. J.P. Chu, J. Jang, J. Huang, H. Chou, Y. Yang, J. Ye, Y. Wang, J. Lee, F. Liu, P. Liaw, *Thin Solid Films* 520 (2012) 5097.
3. D. Li, Z. Zhu, H. Zhang, A. Wang, Z. Hu, *Sci. China Physics, Mech. Astron.* 55 (2012) 2362.
4. Y. Zeng, C. Qin, N. Nishiyama, A. Inoue, *J. Alloys Compd.* 489 (2010) 80.
5. C. Qin, K. Asami, H. Kimura, W. Zhang, A. Inoue, *Electrochem. commun.* 10 (2008) 1408.
6. C. Gutiérrez, C.A. Melendres, Spectroscopic and diffraction techniques in interfacial electrochemistry, Springer Science & Business Media, 2012.
7. A.P. Tafti, A.B. Kirkpatrick, Z. Alavi, H.A. Owen, Z. Yu, *Micron* 78 (2015) 54.
8. R. Ummethala, F. Despang, M. Gelinsky, B. Basu, *Electrochim. Acta* 56 (2011) 3809.
9. F.E.-T. Heakal, K.A. Awad, *Int. J. Electrochem. Sci* 6 (2011) 6483.
10. P. Jakupi, D. Zagidulin, J. Noël, D. Shoesmith, *Electrochim. Acta* 56 (2011) 6251.
11. N. Mahato, M. Singh, *Port. Electrochim. Acta* 29 (2011) 233.
12. M. BenSalah, R. Sabot, E. Triki, L. Dhouibi, P. Refait, M. Jeannin, *Corros. Sci.* 86 (2014) 61.
13. S.T. Arab, K.M. Emran, H.A. Al-Turaif, *Korean Chem. Soc.* 56 (2012) 448.
14. B. Ter-Ovanessian, C. Alemany-Dumont, B. Normand, *Electrochim. Acta* 133 (2014) 373.
15. K. Khaled, *J Appl Electrochem* 41 (2011) 423.
16. K. Khaled, *Electrochim. Acta* 55 (2010) 5375.
17. M. Pourbaix, "*Atlas of Electrochemical Equilibria in Aqueous Solutions*", National Association of Corrosion Engineers, Houston, Texas (1974).
18. A. Rauf, E. Mahdi, *Int. J. Electrochem. Sci* 7 (2012) 4673.
19. D.D. Macdonald, *Electrochim. Acta* 56 (2011) 1761.
20. D.D. Macdonald, *Pure Appl. Chem.* 71 (1999) 951.
21. A.C. Lloyd, J.J. Noël, S. McIntyre, D.W. Shoesmith, *Electrochim. Acta* 49 (2004) 3015.
22. W.A. Badawy, K.M. Ismail, A.M. Fathi, *Electrochim. Acta* 50 (2005) 3603.
23. S. Karimi, T. Nickchi, A. Alfantazi, *Corros. Sci.* 53 (2011) 3262.
24. J. Grosseau-Poussard, J. Dinhut, J. Silvain, R. Sabot, *Appl. Surf. Sci.* 151 (1999) 49.
25. S. Ningshen, M. Sakairi, K. Suzuki, S. Ukai, *Corros. Sci.* 78 (2014) 322.
26. P. Singh, V. Srivastava, M. Quraishi, *J. Mol. Liq.* 216 (2016) 164.
27. S.T. Arab, K.M. Emran, H.A. Al-Turaif, *J. Saudi Chem. Soc* 18 (2014) 169.
28. R. De Oliveira, D. Albuquerque, F. Leite, F. Yamaji, T. Cruz, Measurement of the nanoscale roughness by atomic force microscopy: basic principles and applications, INTECH Open Access Publisher, 2012.
29. B.R. Kumar, T.S. Rao, *Dig. J. Nanomater. Biostructures* 7 (2012) 1881.